

Stress-induced damage evolution in cast AlSi12CuMgNi alloy with one and two ceramic reinforcements. Part II: Effect of reinforcement orientation

S. Evsevlev^a, S. Cabeza^b, T. Mishurova^a, G. Garcés^c, I. Sevostianov^d, G. Requena^e, M. Boin^f,
M. Hofmann^g, G. Bruno^{a,h*}

^a Bundesanstalt für Materialforschung und –prüfung (BAM), Unter den Eichen 87, 12205 Berlin, Germany

^b Institute Laue-Langevin, Avenue des Martyrs 71, 38000, Grenoble, France

^c National Center for Metallurgical Research CENIM-CSIC, Av. Gregorio del Amo 8, 28040 Madrid, Spain

^d Department of Mechanical and Aerospace Engineering, New Mexico State University, Las Cruces, NM 88001, USA

^e German Aerospace Centre, Institute of Materials Research, Linder Höhe, 51147 Cologne, Germany

^f Helmholtz-Zentrum Berlin für Materialien und Energie GmbH (HZB), Hahn-Meitner-Platz 1, 14109 Berlin, Germany

^g Forschungs-Neutronenquelle Heinz Maier-Leibnitz (MLZ/FRMII), Technische Universität München, Lichtenbergstraße 1, 85748 Garching, Germany

^h University of Potsdam, Institute of Physics and Astronomy Karl-Liebknecht-Str.24-25 , 14476 Potsdam, Germany

* Author for correspondence: giovanni.bruno@bam.de

Abstract

While there is a large body of literature on the micro-mechanical behavior of metal matrix composites (MMCs) under uniaxial applied stress, very little is available on multi-phase MMCs. In order to cast light on the reinforcement mechanisms and damage processes in such multi-phase composites, materials made by an Al-based piston alloy and containing one and two ceramic reinforcements (planar-random oriented alumina fibers and SiC particles) were studied. *In-situ* compression tests during neutron diffraction experiments were used to track the load transfer among phases, while X-ray computed tomography on pre-strained samples was used to monitor and quantify damage. We found that damage progresses differently in composites with different orientations of the fiber mat. Because of the presence of intermetallic network, it was observed that the second ceramic reinforcement changed the load transfer scenario only at very high applied load, when also intermetallic particles break. We rationalized the present results combining them with previous investigations and using a micromechanical model.

Keywords

Multi-phase; metal matrix composites; intermetallics; computed tomography; *in-situ* neutron diffraction; piston alloy; load transfer

1. Introduction

Metal matrix composites (MMC) are advanced materials for various applications in automotive and aerospace industries. The addition of ceramic short fibers (SF) [1] considerably improves the strength and creep resistance of Al-Si alloys [2-4]. These SF MMC are usually produced by infiltration of preforms with a random planar orientation of the short fibers. This leads to a highly anisotropic mechanical behavior (see *e.g.*, [5-8]). Such behavior not only depends on the stress direction, but also on the stress sign (tension / compression asymmetry) [5,7].

The addition of SiC particles as a second reinforcement phase helps to improve the wear resistance and fracture toughness of the composite [9-12]. Moreover, based on the results reported in [13] and [14], we may guess that the addition of particles to composites reinforced with ceramic SF could reduce the anisotropy of mechanical properties, without a dramatic loss of creep resistance.

Recently, the microstructure and the mechanical behavior of an AlSi12CuMgNi alloy reinforced with a hybrid preform of 15% vol. of SiC particles and 7% vol. of Al₂O₃ short fiber was reported [15]. This microstructure is characterized by a percolating ceramic preform interconnected by eutectic Si and intermetallic (IM) phases. The mechanical behavior of such materials and the capability of both Si and ceramic phases to reinforce the alloy were analyzed *in-situ* by compression tests during neutron diffraction (ND) experiments *in a direction parallel to the fiber plane*. The results were compared with previous studies on the same alloy reinforced

only with 15% vol. of Al_2O_3 short fiber. A micromechanical model was developed to simulate the evolution of the internal stress of each phase during compression.

In order to further advance the understanding of the load transfer and damage mechanisms in multi-phase composites, with particular focus on Al piston alloy matrices, the present work has manifold objectives: a) To expand the horizons of the study mentioned above [15]. We used *in-situ* ND compression experiments on composites along *a direction perpendicular to the fiber plane* to investigate the load transfer among phases, and synchrotron X-ray computed tomography (SXCT) on plastically pre-strained samples to investigate damage behavior; b) To determine whether and to which extent the hybrid reinforcement induces a more isotropic mechanical behavior in the composite than the pure SF reinforcement. We therefore compared composites with one and two ceramic reinforcements, with alumina fibers in both transverse and parallel orientation to load axis; c) To better quantify the role of intermetallic particles (IM), which were not considered in [15] but have been recently shown to be part of the reinforcement network (see [16]). To this aim, the micromechanical model was extended to include the presence of intermetallic particles, and we show that those particles play an important role in determining the mechanical behavior of these composites; d) To expand the basic knowledge about mechanical properties of multi-phase composites (limited to a few publications, see [17-21]). To this aim, we provide experimental data and modeling rationalization fully considering these materials as four- and five-phase composites.

2. Experimental

2.1 Materials

Squeeze casting AlSi12CuMgNi alloy (Tab. 1) reinforced with 15% vol of Al_2O_3 – Saffil short fibers (Type I) and the same alloy reinforced with 7% vol of Al_2O_3 and 15% vol SiC particles (Type II) were produced as described in [15].

Table 1. AlSi12CuMgNi alloy composition

Element	Al	Si	Cu	Mg	Ni	Fe	Mn	Zn	Ti
wt%	Balance	11-13	0.8-1.3	0.8-1.3	1.3	0.7	0.3	0.3	0.2

In the Type I composite, the alloy was cast and infiltrated in a planar-random oriented Al₂O₃ short fibers preform (fiber mats). In case of Type II composite, the preform contained also SiC particles in-between the short fibers. The cylindrical samples under study were obtained by electrical discharge machining (EDM) of the cast billets with the planes of randomly oriented fibers perpendicular to the rotation axis. The samples were therefore tested with the fiber planes *orthogonal* to loading direction (and labelled _O, to distinguish them from our previous work [15], where samples with the fiber planes *parallel* to loading direction (_P) were investigated, see below).

2.2 Compression tests

The uniaxial compression test at room temperature was carried out to evaluate the macro-mechanical behavior of the composites. The strain rate in a universal tensile MICROTTEST rig with a load cell of 20 kN was set to 10^{-4} s^{-1} . Cylindrical samples with length of 8 mm and diameter of 4 mm were used.

2.3 3D microstructural characterization

Synchrotron X-ray computed tomography (SXCT) was carried out in order to disclose damage after compression tests, *i.e.* in pre-strained samples. Samples after uniaxial compression were trimmed down to 1.5mm diameter by EDM to be able to achieve the highest possible resolution (smallest pixel size). Measurements were performed at the BAMline beamline (BESSY II, HZB Berlin, Germany) [22]. The energy of the monochromatic X-ray beam was set to 25keV and a pixel size of $0.44 \times 0.44 \mu\text{m}^2$ was achieved using a commercially available system (Optique

Peter) with 10x Olympus microscope objective and PCO 4000 CCD-based camera. The reconstruction of 3D volumes from single projections was made by means of a BAM in-house-developed filtered back projection software, and a single-distance phase-contrast correction algorithms [23] using ANKA phase software [24]. AvizoFire® software was used for segmentation of the different phases (*i.e.* different grey values) and for visualization of the reconstructed volumes. The volume fractions of the different phases as obtained by SXCT have been reported elsewhere [25,15]. To estimate the amount of damage in the samples, volume fractions of damage-related voids were obtained from the average of 3 sub-volumes ($440 \times 440 \times 220$) μm^3 , providing the standard deviation among these measurements as experimental error. The total volume fraction of damage-related voids only includes features that could be segmented (*i.e.* whose size lies above the resolution limits).

The interconnected reinforcing network was also analyzed in several pre-strained samples, whereby the aluminum matrix had been chemically removed. The deformed samples were chemically deep-etched using a solution of H₂O and HCl with a volume ratio of 80:20 during 90 min. The deep-etched samples were then studied in a HITACHI S-4800 scanning electron microscope (SEM).

2.4 In-situ neutron diffraction

Cylindrical samples with 12 mm length and 6 mm diameter were used (machined following the same procedure described above). The axial strain component (ϵ_1) and the radial component (ϵ_3 , assumed to be in-plane isotropic) were measured along the corresponding scattering vectors (Figure 1) for each composite and phase, as described below.

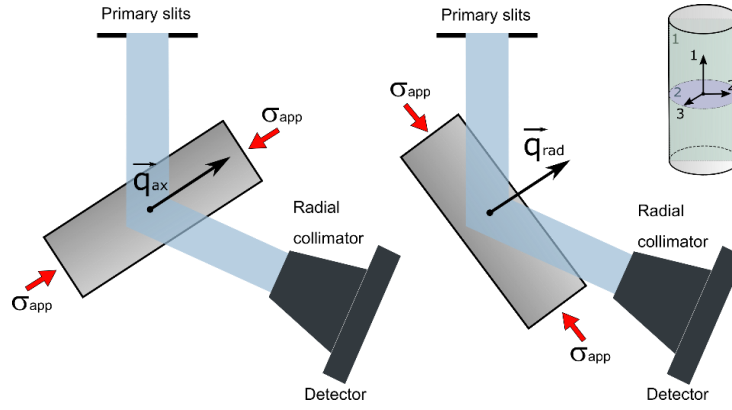


Figure 1. Set up for ND and *in-situ* compression experiment (q scattering vector for axial and radial components). Axial -1 and radial -2 or 3- directions are given in the sample with respect to the fiber plane orientation (in 2).

The *in-situ* ND experiments were conducted at two neutron beamlines: STRESS-SPEC (FRM II, Munich, Germany) and E3 (BERII, HZB, Berlin). The details of the measurements at E3 can be found in [15]. The STRESS-SPEC beamline provides a monochromatic beam, and a wavelength $\lambda=1.672 \text{ \AA}$ was chosen. The nominal gauge volume within the sample, defined by an incident beam slits and a radial collimator, was of $4 \times 4 \times 5 \text{ mm}^3$. The evolution of volume-averaged lattice strains with the applied load was determined through the shift of the position of Al-311, Si-422, and hexagonal SiC-116 reflections (at Bragg angles $2\theta = 86^\circ, 98^\circ, \text{ and } 79^\circ$, respectively) as a function of the applied load. The diffraction peak of the alumina short fibers suffered a broadening effect due to their nanocrystalline (and partially amorphous) nature and did not provide a reliable fit to obtain the peak position. The specimens were compressed step-wise using an in-house-built load-rig with a load cell of 50 kN. The axial and radial components were measured with a single sample mount [26]. For each loading step, both radial and axial directions were measured acquiring for 3min Al and SiC peaks (recorded at the same detector position), and for 15 min the Si peak. For measurements within the Al-matrix elastic region, identified by previous diffraction experiments [25,15] (data measured at E3 beamline reported also here), the rig was driven in load control, while in the plastic regime of Al the rig was driven

in displacement control with a step of 0.08 mm. In this way, similar strains were achieved for all samples. During unloading four points were measured in the load control mode.

A stress-free reference is required for the calculation of absolute internal strains. For the investigated multiphase material, the reliable unstrained sample of every phase was unavailable: the powders of the alloy would contain the percolating network of the Si and aluminides; dissolution of the Al matrix and aluminides could not yield the Si phase alone, most probably because of a chemical reaction among phases. Finally, the raw SiC reinforcement was not available. Therefore, for each phase, we calculated stress differences using the following equation:

$$\sigma_1 - \sigma_3 = -\frac{E}{1+\nu} (\theta_1 - \theta_3) \cot \theta_0 \quad (1)$$

where σ_1 and σ_3 are the principal stresses, E is Young's modulus, ν is Poisson's ratio, θ_1, θ_3 are measured Bragg's angles along the corresponding sample directions, and θ_0 is the reference Bragg angle ($\theta_0 = \theta$ at the pre-load condition of -20MPa).

Table 2. Diffraction Elastic Constants of the different phases used in micromechanical modelling.

Phase	E (MPa)	G (MPa)	Poisson's Ratio
Al 311	69.4	25.93	0.35
Si 422-cubic	167.35	69.96	0.215
SiC 116-hex	430		0.175
Al ₂ O ₃ fibers	300	125	0.2
Intermetallic	148	-	0.32

The plane-specific diffraction elastic constants used for the calculation of stresses are reported in Tab.2. They were calculated using XEC software [27] and adopting a Kröner model [28]. All materials have random crystal structure. Although the stresses in alumina short fibers were not

experimentally measurable, the stress differences for this phase (combined with those in the intermetallic phases) could be obtained from the stress balance condition [29], taking into account the volume fraction f for each phase, which for the 4-phase composite reads:

$$\sigma_{app} = [1 - f^{Si} - f^{SiC} - (f^{Al_2O_3} + f^{IM})] \cdot (\sigma_1^{Al} - \sigma_3^{Al}) + f^{Si} \cdot (\sigma_1^{Si} - \sigma_3^{Si}) + f^{SiC} \cdot (\sigma_1^{SiC} - \sigma_3^{SiC}) + (f^{Al_2O_3} + f^{IM}) \cdot (\sigma_1^{Al_2O_3+IM} - \sigma_3^{Al_2O_3+IM}) \quad (2)$$

3. Results

3.1 Macro-mechanical properties

True Stress-True Strain curves for both Type I and Type II composites are presented in Figure 2. For reference, also the curves for the matrix alloy and for both composites with the fiber plane oriented *parallel* to the compression axis (Type I_P and Type II_P, see [15]) are reported. Type II_P composite showed a lower yield stress than Type I_P in spite of the higher total ceramic reinforcement, since the volume fraction of short fibers was 7% instead of 15%vol. This demonstrates the effectiveness of fibers to strengthen the composite, if oriented parallel to the load axis. For Type II_O (fibers orthogonal to the load axis) a yield stress similar to Type II_P is observed (nearly isotropic behavior), in contrast with the significant difference found between Type I_O and Type I_P (see the values in Figure 2). This demonstrates that the addition of SiC particles plays a major role in rendering the mechanical properties of such material nearly isotropic. In the plastic region, composites with fiber plane parallel to the load axis present slightly decreasing work hardening with increasing applied load. As for the orthogonal orientation, in the plastic region both Type I and Type II composites show an almost constant stress up to failure (nearly perfect plastic behavior). Barreling was observed at high strains for both Type I_O and Type II_O composites. The strain to failure for Type I_O and Type II_O is nine and six times higher than for Type I_P and Type II_P, respectively. This indicates a more catastrophic breakage (very small strain hardening was observed) of composites with the fiber plane parallel to the load axis.

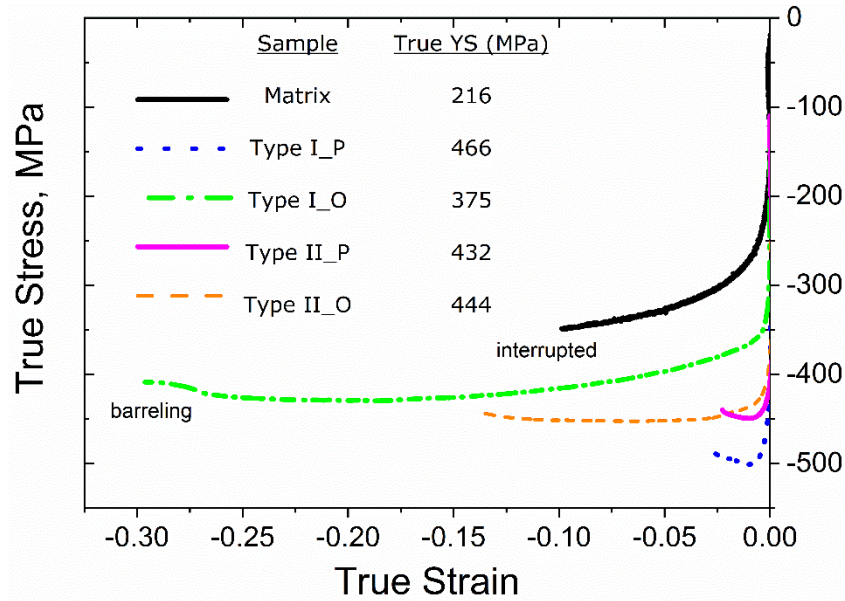


Figure 2. True-stress true-strain curves from *ex-situ* compression tests of different composites and fiber orientations. Matrix alloy is given as reference. Note that the test on the matrix was interrupted before rupture, and that Type I_O suffered from barreling, *i.e.* cannot be taken as quantitatively reliable.

3.2 Damage characterization

Direct observation of damage after compression tests is shown in Figure 3 for Type II_O material. SXCT data for all other materials have been reported elsewhere [25,15], and only some aspects of their quantitative analysis will be used here. Short Al₂O₃ fibers as well as SiC particles appear in light grey (only distinguishable by their shape), eutectic Si in dark grey, intermetallics (~5% vol) in white. Sporadically, some pores related to the fabrication process are present in the Al-matrix. The volume fraction of the initial porosity (in as-cast condition) is less than 0.05%.

For a pre-strained condition of Type II_O similar to the failure strain of Type II_P, (Figure 3a, $\epsilon \sim -2\%$) only a small amount of damage was observed. Damage (in the form of damage-related voids) is observed in all reinforcement phases of the material, but not in the Al matrix: voids appear in the Al₂O₃ short fibers, eutectic Si, IM particles, and in SiC clusters (as shown in the insert in Figure 3a). After failure, *i.e.*, $\epsilon \sim -12.8\%$ (Figure 3b), a large number of voids (related

to cracking) is present in the Al_2O_3 fibers -always perpendicular to the fiber axis-, and in the intermetallic particles. Micro-cracking appears in SiC clusters leading to de-bonding of some particles from the matrix. In the load plane (1) micro-cracking of SiC clusters is more evident and some fibers protruding out of the fiber mat plane are also cracked. The total volume fraction of segmented voids at failure is around 7% (this corresponds to the number of damage-induced voids, since the initial porosity is negligible).

For the pre-strained Type II_O composite direct damage observation was also made by SEM (Figure 4) on specimens deep-etched after testing. Three cylindrical sister samples with a diameter of 5 mm and height of 10 mm were compressed up to a strain of -1.6%, -2.7% and -8% using the load rig and the loading parameters described in section 2.2. After matrix removal (see above), the resulting SEM images for the plane orthogonal to the load direction (plane 2 in Figure 1) are shown in Figure 4. Breakage of fibers, Si and IMs is observed in all pre-strained samples, but to a different amount. The sample pre-deformed to -1.6% plastic strain (Figure 4a) shows a small number of voids. It can be seen that the eutectic Si builds bonds between SiC particles (Figure 4a, b) and alumina fibers, creating additional interconnectivity. Those bonds are not damaged at low pre-strain (Figure 4a). A more significant amount of damage is visible in the sample with -4.9% pre-strain. The main contributions to damage are voids in the bonds built by eutectic Si between ceramic reinforcements (Figure 4c) and breakage of Al_2O_3 fibers. Sporadically, voids (created by cracking) can also be found in SiC particles (indicated by red circles in Figure 4c). The specimen in a condition close to failure (-8% plastic pre-strain) shows a significant fragmentation of alumina fibers, Si and IM particles (Figure 4d).

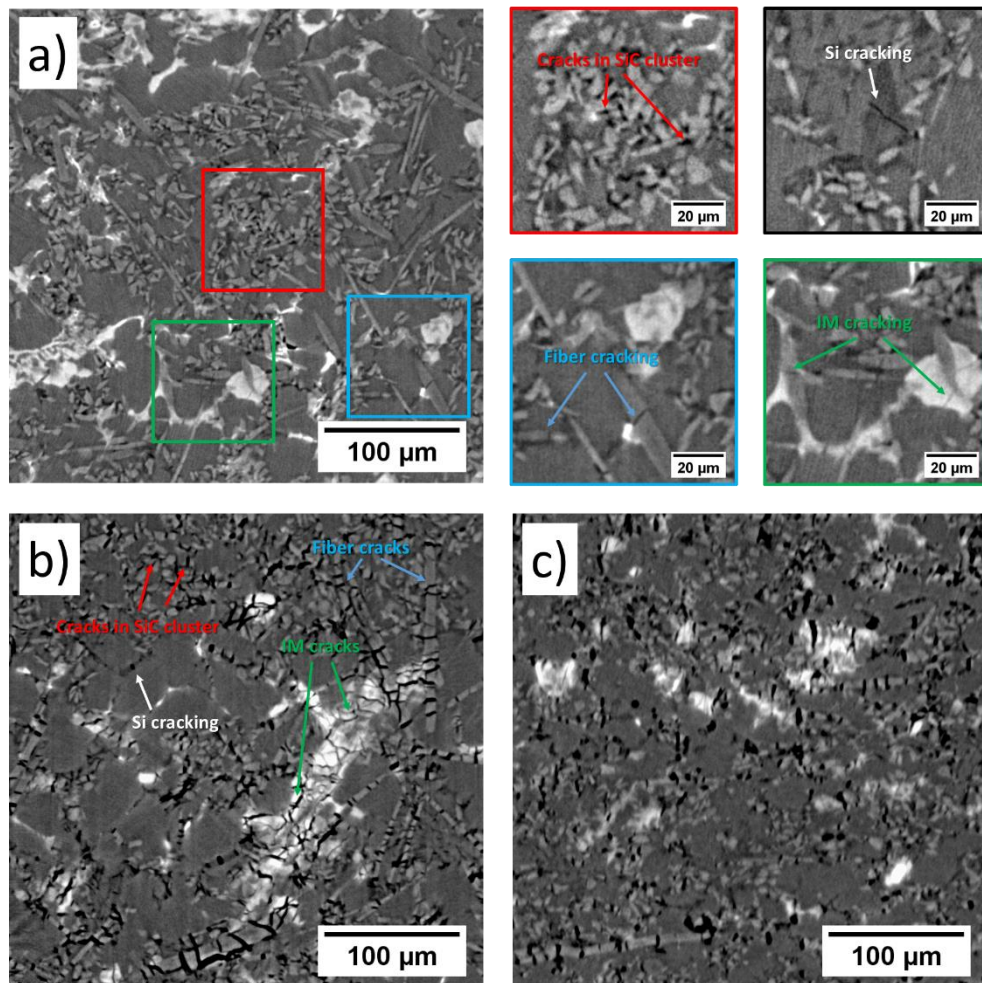


Figure 3. SXCT reconstruction slices for Type II_O material after compression (a) at $\epsilon = -2\%$; (b) at $\epsilon = -12.8\%$ (failure) for a transversal section (in the plane of Al_2O_3 short fibers); (c) at $\epsilon = -12.8\%$ for a section orthogonal to the plane of Al_2O_3 short fibers.

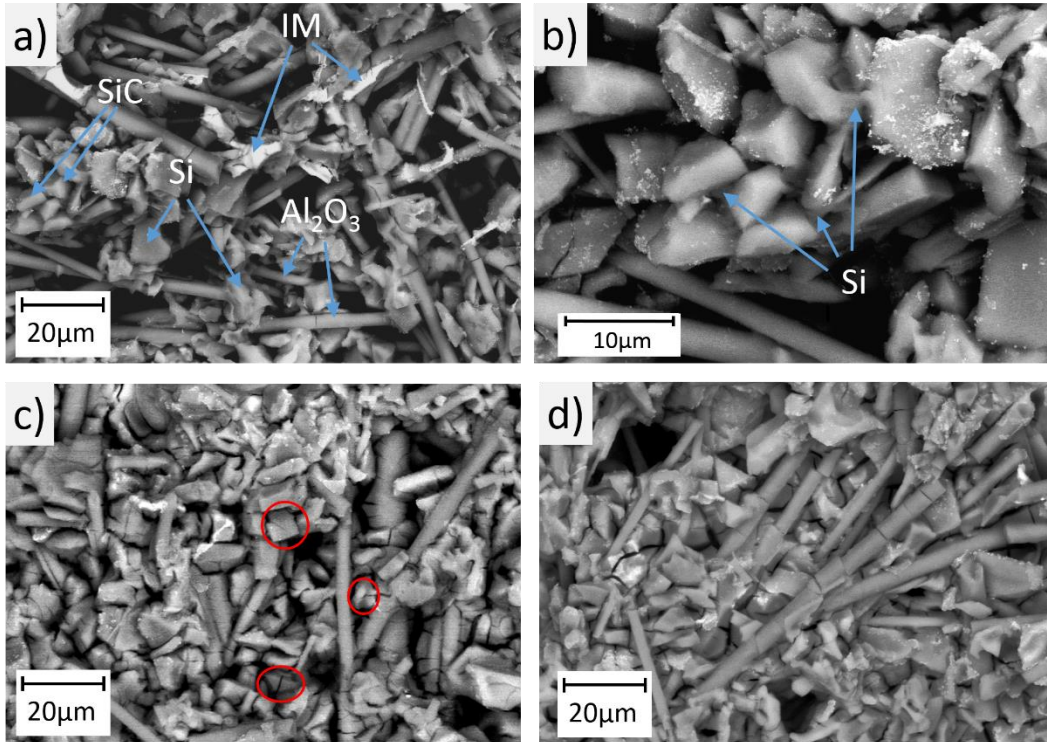


Figure 4. SEM images of etched Type II_O samples in different pre-strain condition: a) $\varepsilon = -1.6\%$; b) enlarged view of the sample pre-strained up to $\varepsilon = -1.6\%$; c) $\varepsilon = -4.9\%$; d) $\varepsilon = -8\%$.

3.3 In-situ neutron diffraction

We used the initial unloaded condition as reference for each phase ($\varepsilon_1 = \varepsilon_3 = 0$). The *in-situ* evolution of phase-specific principal lattice strains (ε_1 and ε_3) during compression tests of Type II_O are reported in Figure 5. Data from similar measurements on E3 at BER II (HZB, Berlin) [25,15] are added for comparison, since they extended further into the plastic region (for Type I_O until failure, and therefore without unloading). Note that the E3 ND measurements were entirely performed under load control, in contrast with the load-displacement control combination at STRESS-SPEC.

As a result from compression loading, with increasing applied stress (*i.e.* applied *composite* stress) there is a general tendency to a decrease of the axial strain (ε_1) for all measured phases, while the evolution of the radial strain (ε_3) is strongly related to the load transfer among phases, rather than to the bare Poisson's effect (especially in the matrix). For the Al-phase (Figure 5a,

c) ε_1 increases linearly until an applied stress about -80 MPa for Type I_O or -100MPa for Type II_O. This implies a significantly lower yield limit than that found from the macroscopic behavior of the two composites and the matrix (see Figure 2). We infer that ND discloses the separate behavior of the Al phase, analogous to previous observations for _P samples [15]. After yielding, the Al-phase ε_1 curve shows a monotonic decrease with a particular step at -200 and -230MPa for Type I_O and II_O, respectively. Type I_O presents more effective hardening than Type II_O until -300MPa (*i.e.* higher slope). This is attributed to a higher volume fraction of reinforcement in Type II (larger load transfer from Al to other reinforcing phases). Above -350MPa, ε_1 in the Al-phase of Type I_O increases rapidly, whereas for Type II_O similar tendency as before is observed. This has been explained (see [6,5,15,25,30]) by a load transfer back to the Al matrix (lattice planes with lower Schmidt factor start sliding) when damage takes place. In the radial direction, the evolution of ε_3 in all phases is constrained by the presence of Al₂O₃ fibers and remains nearly constant. Note that it would be incorrect to extract any sort of “Poisson’s ratio” from the ratio between the radial and the axial data, because of the complex load transfer scenario.

Upon unloading, the lattice strain evolves in a linear fashion in both the axial and the radial directions (but with opposite slopes). After unloading, we observe additional tensile residual strain in the axial direction and compressive in the radial. This agrees with previous observations in Al-matrix composites [6,31,32].

The Si-phase (Figure 5b, d) shows upon loading a mirror evolution pattern of axial and radial strain. This would imply a “microscopic Poisson’s ratio” near to -1; this effect is correlated to the reinforcement geometry, whereby the fibers play a dominant role in the load transfer (especially in their preferential plane 3). Upon unloading, a hysteresis can be observed for the radial direction, while lattice strains in the axial direction recur nearly the same curve for both Type I_O and II_O. Damage is inferred from the loss of load carrying capability, represented

as a decrease of slope for Type I_O above -350 MPa and for Type II_O above -400 MPa. After unloading, the radial direction accumulates additional tensile RS, while the axial direction returns (nearly) to the initial point for both composites.

The evolution of strains in the SiC phase shows a similar behavior to that of the Si phase. At high applied stress, micro-cracking in the SiC clusters (visible in Figures 3b and 4c, d) is reflected by a sudden drop in ε_1 at about -350 MPa upon loading. Some hysteresis is visible for the radial direction, while in the case of the axial direction the final state (after unloading) coincides with the initial one.

The macroscopic displacement given by the load rig during measurements at the E3 beamline is shown in Figure 6 to show the onset of the plastic region in the two composites. This displacement cannot be translated into strain, since the contribution of the machine compliance is unknown. The *in-situ* compression test at STRESS-SPEC was done only for the microscopic elastic region for both composites. For this case the stress-displacement curve is not even available. However, the lattice strain evolutions in Figure 5 prove a good correlation between the results obtained on the two beamlines.

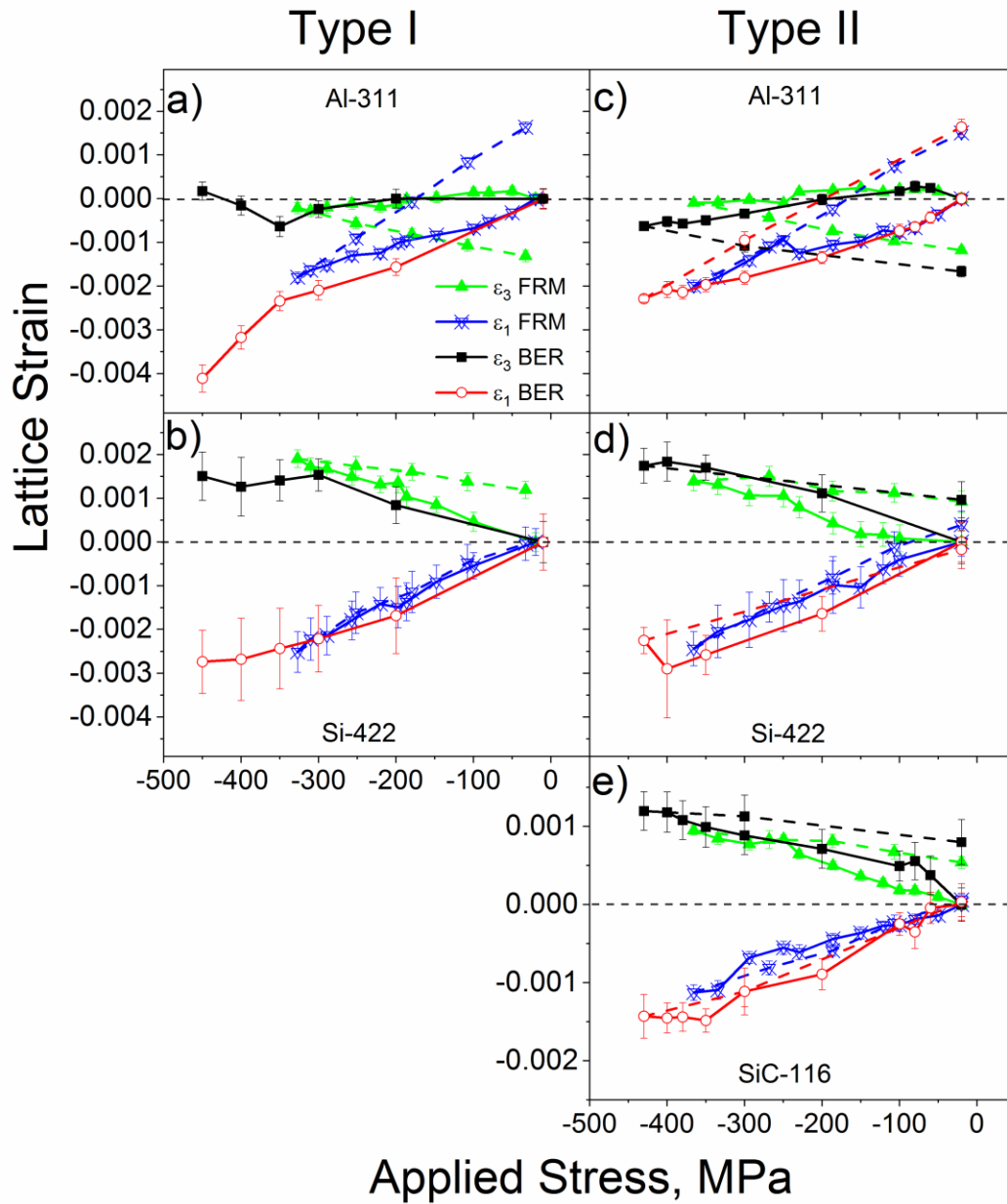


Figure 5. Lattice strain evolution upon compression for two composites Type I_O (left), Type II_O (right) of Aluminum phase (a) (c); Silicon phase (b) (d); SiC particles (only in Type II_O) (e). The unloading pattern is plotted with dashed lines.

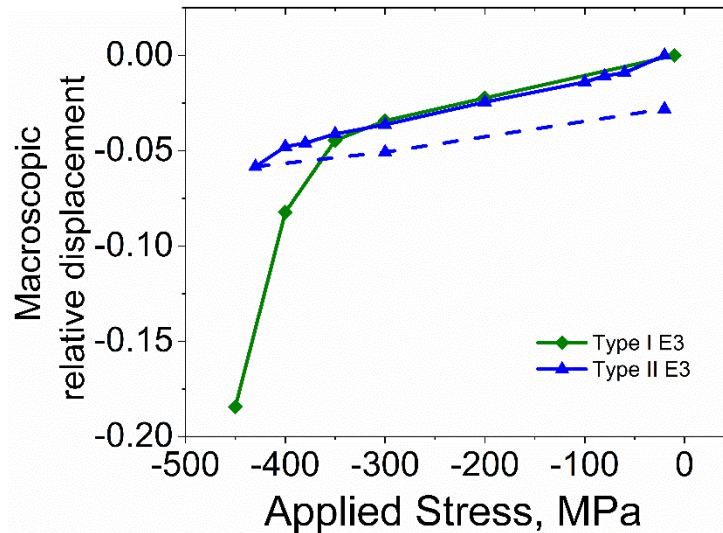


Figure 6. Macroscopic relative displacement from load rig during *in-situ* experiment at E3 beamline. The dashed line corresponds to unloading

3.4 Modelling of mechanical behavior

Micromechanical modelling is usually applied for calculation of the overall properties of heterogeneous materials. In particular, the approach based on Maxwell's homogenization scheme has proved to be accurate [33]. As shown in [25,34,15], the same approach can be used to describe the average stress of individual phases in composites. This approach accounts for matrix plasticity, possible fragmentation of the inhomogeneities during loading, and interaction among the inhomogeneities. The accurate quantitative information about the fragmentation process as a function of applied stress would require cumbersome *in-situ* CT measurements. These are certainly desirable but are left for further work. Here we exploited our *ex-situ* CT data and modelled fragmentation assuming a linear dependence of damage accumulation on applied stress. The shape of the phases and the damage mechanisms for both composites are schematically shown in Figure 7. The model was improved from previous versions by additionally introducing failure of intermetallic particles and by adjusting the onset of Al plasticity to -100 MPa from ND experiments (previous -200 MPa from macroscopic behavior [15]). In the model calculations we took nominal values for the volume fractions of Al_2O_3 fibers

and SiC particles and calculated volume fractions by SXCT for eutectic Si and IMs, reported in [15].

The two materials were modeled as multiphase transverse-isotropic composites consisting of a continuous aluminum alloy matrix and three or four families of inhomogeneities (respectively, Type I and II).

Type I Composite:

(1) Saffil Al_2O_3 fibers with an average aspect ratio of 40 were randomly oriented in the plane determined by directions 2 and 3 and had a volume fraction of 15%. The damage of fibers was introduced by reducing their aspect ratio. The variation of the aspect ratio was assumed linear between an initial value of 40 at the applied stress of -360 MPa and a final value of 3 at the applied stress of -460 MPa. The aspect ratio at the final loading step was set on the base of the large amount of damage observed in the SXCT data [25]. The decrease of the aspect ratio of fibers simulated their fragmentation from prolate rods to almost spheroidal particles (Figure 7a).

(2) The eutectic silicon phase was modeled by randomly oriented oblate spheroids with the aspect ratio of 0.15, and a total volume fraction of 7% (determined by SXCT data). The damage of eutectic Si particles observed in the SXCT and SEM data was introduced by linearly varying the aspect ratio as a function of load. Onset of damage was assumed to occur at the applied stress of -360 MPa (see Figures 4 and 5). The maximum aspect ratio of Si particles was set to 1 (spherical particles) at the applied stress of -460 MPa (Figure 7b).

(3) Intermetallic primary phases were modeled as concave particles (see the flaky, star-like shapes in Figure 4a and in the SXCT reconstructions) with aspect ratio of 1. Their volume fraction was 5.5% (determined by quantitative image analysis of SXCT data). Similar to the case of Si and Saffil Al_2O_3 fibers, a variable aspect ratio accounted for the IM particles fragmentation. The first instance of damage in IM particles was assumed to occur at the applied

stress -360 MPa, followed by a decrease of the aspect ratio up to a minimum of 0.2 at -460 MPa (Figure 7c).

Type II Composite:

(1) Saffil Al_2O_3 fibers we modelled with the same shape and spatial distribution as in Type I composite but a volume fraction of 7%. According to the SXCT data (see discussion below) the damage in Type II composite occurs at a higher applied load than in Type I composite. In fact, as we will see later, CT data imply that the damage rate as a function of strain is much larger for Type I composite.

The onset of damage in the fibers was assumed at -380 MPa, followed by a decrease of the aspect ratio down to 20 at the applied stress -450 MPa (Figure 7a).

(2), (3) For the eutectic silicon phase and IMs we used the same volume fractions and initial aspect ratios as for the Type I composite. The volume fractions of Si and IMs were calculated from the available SXCT data. The first damage in eutectic Si and IMs was assumed to occur at the applied stress of -380 MPa. Similar to alumina fibers, we assumed a lower amount of damage (fragmentation of phases) in the Si and IM phases of Type II_O composite. The final value of the aspect ratio at the maximum applied stress of -450 MPa was set to 0.35 for Si and to 0.5 for IMs (Figure 7b, c).

(4) Polyhedral SiC particles (volume fraction 15%) form interconnected clusters, clearly seen in Figure 3a and 4b. These clusters have rather irregular shapes that are difficult to model in a unified way. In the model, the variety of these shapes is described with sufficient accuracy by prolate spheroids of aspect ratio 8. For the pre-strained sample (-2% strain) it was shown that the damage is initiated as micro-cracking among SiC particles splitting the clusters. Taking this into account, the aspect ratio is varied linearly from 8 in the initial condition to 5 at the applied stress of -450 MPa (Figure 7d).

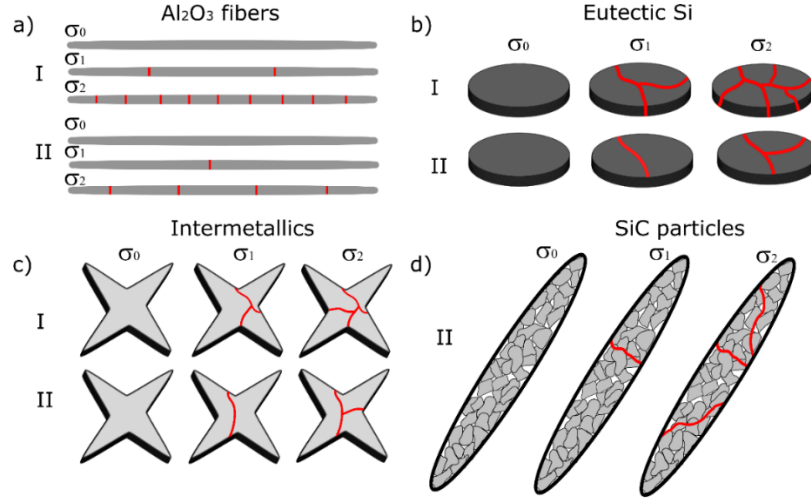


Figure 7. Schematic shape of phases and damage mechanism in Al₂O₃ fibers (a), eutectic Si (b), intermetallics (c) and clusters of SiC particles (d) in Type I and Type II composites.

Note that $\sigma_0 < \sigma_1 < \sigma_2$ represent different levels of applied stress.

The elastic properties of the Al, Si and ceramic reinforcements are given in section 2.4 (see Tab.2). For the following IM phases: Al₇Cu₄Ni, Al₂Cu, FeNiAl₉, previously identified in the investigated alloy [35], a (global) macroscopic Young's modulus $E_{IM} = 148$ MPa is calculated based on the nano-indentation results reported in [36]. The (global) Poisson's ratio for IMs is taken to be equal to 0.32.

According to the *in-situ* ND experimental data (Figure 5) the onset of plasticity of the Al occurs at $\sigma^{app} = -100$ MPa. Changes in mechanical properties of the Al are introduced through identification of a tracking parameter [37], in this case σ^{app} . The shear modulus of the material is varied as a function of σ^{app} according to:

$$G_0(\sigma^{app}) = G_0(0) - \frac{T}{\pi} \left[\arctan\left(\frac{\sigma^{app} - \sigma_y}{h}\right) - \arctan\left(\frac{\sigma_y}{h}\right) \right] \quad (3)$$

where $G_0(0)$ is the shear modulus prior to loading, σ_y is the yielding point, and parameters T and h determine the character of the variation of the shear modulus in the process of loading. The following parameters were used in the simulation: $G_0(0) = 25.93 \text{ GPa}$, $\sigma_y = 100 \text{ MPa}$, $h = 12 \text{ MPa}$ and $T = 24 \text{ GPa}$. Note that while the use of the *arctan* function to describe the evolution of the stress-strain curve may seem arbitrary, but it just reflects the necessity of having an analytical function that can be used as input in the (analytical) model. Any other function fitting well the experimental data can be used without loss of validity (and generality) of the model. We also remark that, while the parameters G_0 , σ_y , h and T may seem experiment-specific, they are indeed material-related as long as the stress-strain curves of Al are reproducible. The average stress $\bar{\sigma}^{(i)}$, over phase i is given by the stress concentration tensor $\mathbf{\Gamma}$, which has been introduced for inhomogeneities of arbitrary shape by Hill [38].

$$\bar{\sigma}_{kl}^{(i)} = \Gamma_{klmn}^{(i)} \sigma_{mn}^{\text{app}} \quad (4)$$

where σ^{app} is the stress tensor acting on the whole sample. Note that for a multiphase composite material consisting of $N+1$ phases with volume fractions φ_0 (matrix), φ_i ; $i = 1, \dots, N$ (reinforcements), satisfying the condition $\varphi_0 + \sum \varphi_i = 1$, the identity $\varphi_0 \Gamma^0 + \sum_i \varphi_i \Gamma^i = J$ holds (where J is the fourth-rank unit tensor). Tensor Γ^i for an isolated spheroidal inhomogeneity with semi-axes $a_1 = a_2 = a$, a_3 has been calculated by Wu [39] as a function of the aspect ratio $\gamma = a/a_3$. The components of this tensor are given in the Appendix. As shown by [40], the contribution of a *concave* inhomogeneity to the overall elastic properties and stress concentration in the inhomogeneity can be described with sufficient accuracy by a product of Γ^i for a circumscribed spheroid and a multiplier

$$\eta(p) = \frac{3\pi}{4} \frac{(5p-1)p^2 \Gamma(3m)}{\Gamma(m)^3} \quad (5)$$

where $p \leq 1$ is concavity factor and $\Gamma(p) = \int_0^\infty e^{-t} t^{p-1} dt$ is Gamma function (not to be confused with the tensor Γ). For intermetallic precipitates the concavity factor is taken as $p=0.35$. Note that the value of $p=0.5$ corresponds to the boundary between concave and convex shapes. To calculate phase-average stresses, an average over the orientation of each phase is performed (see Appendix).

To take the interaction between inhomogeneities into account, any variant of the so-called effective field method (where each inhomogeneity, treated as isolated one, is placed into a uniform effective field that differs from the remotely applied one) can be used. As it has been shown in [15,34] the best agreement with the experimental data is given by Maxwell scheme [41] in the interpretation given in [33] and [42]. In the context of the calculation of phase-average stresses, equating these two quantities leads to the following formula (see [34] for further details):

$$\langle \boldsymbol{\sigma} \rangle_{ij}^p = \left(\bar{\Gamma}^p \right)_{ijkl} A_{klmn} \sigma_{mn}^\infty \quad (6)$$

where collective interaction between all inhomogeneities in the composite is described by

A_{klmn} - fourth rank tensor inverse to $\left[\mathbf{J}_{ijkl} - \mathbf{Q}_{ijmn}^\Omega \sum_p \varphi_p \left(S_{mnrst}^{(p)} - S_{mnrst}^{(0)} \right) \bar{\Gamma}_{rst}^{(p)} \right]$. Here, $S^{(p)}$ is the

compliance tensor of the p -th family of inhomogeneities, S^0 is the matrix compliance, \mathbf{J} is the 4-th rank unit tensor. Components of tensor \mathbf{Q}^Ω are given in the Appendix. The list of all parameters used in the model is given in Table 3.

Table 3. List of parameters used in the micromechanical model.

Parameter	Value	Source	Sensitivity of model prediction	Reproducibility
Volume fraction of Al ₂ O ₃ fibers, SiC particles	Type I: 15 vol.%; Type II: 7 vol.%; 15 vol.%	Producer specification	Low	Moderate
Volume fraction of eutectic Si, IM phase	Type I and II: 7 vol.%; 5.5 vol.%	Computed tomography	Low	Moderate
Aspect ratio of Fibers, Si, IMs, SiC particles	see above.	Adjusted in the range, evaluated from the computed tomography and SEM micrographs	Moderate	Moderate (CT data)
Concavity of IM particles	0.35	Adjusted in the range, evaluated from computed tomography	Moderate	Moderate
The variation of the shear modulus	h=12 MPa T=24 GPa	Evaluated from the macroscopic experiments	High	High
Elastic properties of the phases	see Table 2	XEC software, literature values	High	Moderate

The onset of damage for different phases occurs for the same applied stress but indeed corresponding to different phase-specific stress.

Figure 8 shows the comparison between the experimental data (Figure 5) and the predictions provided by the Maxwell scheme for the principal stress differences in the two composites, neglecting any residual stress. Since Al₂O₃ fibers are randomly oriented in a plane orthogonal to the load axis, cylindrical symmetry conditions were applied, *i.e.* $\sigma_2 = \sigma_3$. Consequently, in the axial plane (the plane of transverse isotropy): $\sigma_1 - \sigma_2 = \sigma_1 - \sigma_3$. It is seen that the predictions of Maxwell scheme are in the range of the experimental error until $\sigma^{app} = -400$ MPa. Stress differences become more compressive with increasing compressive applied load. They show elastic, plastic and damage regions: In the case of Al-phase, the onset of plasticity is again visible at $\sigma^{app} = -100$ and -80 MPa for Type I_O and Type II_O, respectively (Figure 8a, c).

The proposed micromechanical model reproduces well the elastic and plastic region for Type I_O, whereas for Type II_O some discrepancy appears above $\sigma^{\text{app}} = -400$ MPa, where the Al phase stress starts being constant (loss of load carrying capability). Also for Si-phase (Figure 8b, d) the model slightly deviates from the last experimental points: this is due to the occurrence of damage and might be attributed to the effect of the Si percolating geometry (also not considered in the model). Finally, the stress difference in the SiC phase follows the experimental data showing a linear behavior up to the applied stress of approximately -360 MPa. Then a small decrease of the slope occurs (also caught by the model), indicating the damage initiation in the SiC phase. Model predictions lie in-between the two available sets of experimental data, and therefore agree well with both.

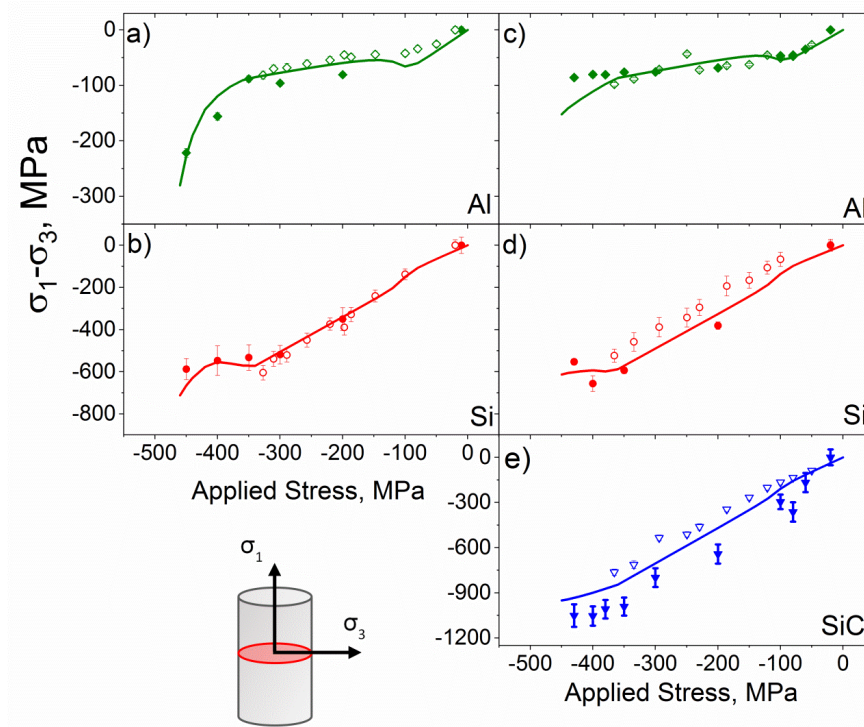


Figure 8. Comparison of experimental (points) and modeled (lines) stress differences for Type I_O: a) Al, b) Si; for Type II_O: c) Al, d) Si, e) SiC. The full points present experimental results from E3 and the hollow ones from STRESS-SPEC.

In Figure 9, the stress differences in Al_2O_3 fibers and intermetallic phases calculated by stress balance (Eq. 2) of experimental data are compared with those simulated by using the Maxwell

scheme. The sum of volume fractions of the two phases was 20.5% for Type I and 12.5 % for Type II (hollow points for STRESS-SPEC, full for E3). The different volume fraction of the reinforcement phases in the two composites strongly impacts the final stress values.

The model provides the separate stress differences for Al_2O_3 (green dashed) and intermetallics (pink dot-dashed - IM), as well as the combined value, which was calculated by the rule of mixture (black solid line):

$$\sigma_{\text{Al}_2\text{O}_3+\text{IM}} = \frac{f_{\text{Al}_2\text{O}_3}}{f_{\text{Al}_2\text{O}_3}+f_{\text{IM}}} \sigma_{\text{Al}_2\text{O}_3} + \frac{f_{\text{IM}}}{f_{\text{Al}_2\text{O}_3}+f_{\text{IM}}} \sigma_{\text{IM}} \quad (7)$$

The model fits fairly well to the experimental data belonging to the combination of Al_2O_3 and IM. It predicts that the fibers would carry more load (higher slope) than IM in both materials (Figure 9a, b). However, for Type I_O Al_2O_3 fibers present significant damage at high loads (decreasing the reinforcement capability in radial direction), and IM would take over part of the load (increasing slope of the curves in Figure 9). In the case of Type II_O (Figure 9b) the experimental points do not follow a linear trend, evidencing simultaneous damage of both phases and load transfer among them. It is impossible to distinguish the two contributions in the plots of Figure 9b and Figure 8. It can be clearly seen that part of the load from damaged Si and SiC particles is carried by fibers and IMs and is not transferred back to Al at high loads, contrary to the case of Type I_O composite (ref. the constant slope in Figure 8c and increase of the slope of the Al-stress vs applied stress curve in Figure 8b).

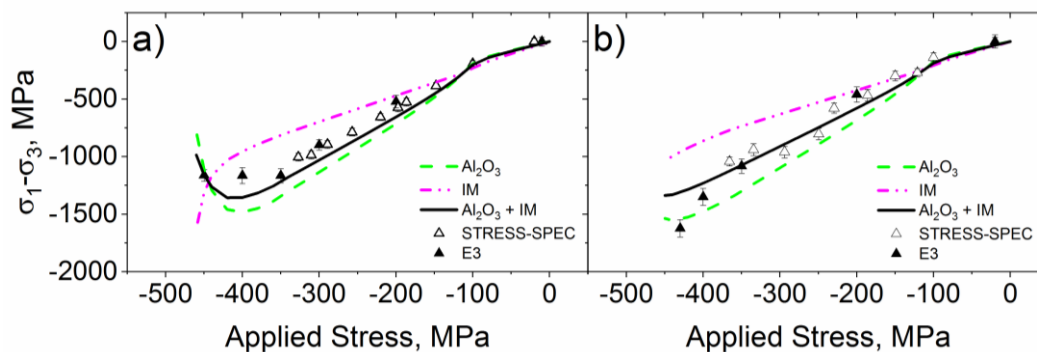


Figure 9. Comparison of stress differences calculated from stress balance of experimental data for Al₂O₃ and IM (points) and modelling results (lines) for (a) Type I_O and (b) Type II_O.

4. Discussion

Previous studies on Type I composite showed different damage scenarios depending on the reinforcement orientation [25] and on the type of reinforcement (_P case) [15]. For the matrix alloy, Si and intermetallic phases were broken, whereas only Si was damaged for the composite with Al₂O₃ in parallel configuration (Type I_P) [25]. In contrast, when the configuration of Al₂O₃ short fibers is orthogonal to the applied load axis (Type I_O), these fibers are heavily cracked and behave as a particle reinforcement (where the Al-matrix takes over part of the load). When adding SiC particles in the parallel configuration of Al₂O₃ short fibers (Type II_P) [15], micro-cracks initiate between particles in SiC clusters.

Figure 10 presents the comparison between the microstructures of Type II composites with different fiber orientations (_O and _P). Note that, as mentioned in section 3.2, the initial volume fraction of pores in the SXCT reconstructed volumes is less than 0.05% for both composites and the void fraction corresponds to damage created by the applied pre-strain. There is a large number of interconnected voids in Al₂O₃ for Type II_O (Figure 10b), whereas for Type II_P (Figure 10c), voids are isolated, and the amount of damage is lower. Since Al₂O₃ are brittle ceramic fibers, tensile loads are particularly detrimental to their integrity. Under uniaxial compression, fibers orthogonal to the applied stress (Type II_O) will therefore more likely break than fibers parallel to the applied stress (Type II_P).

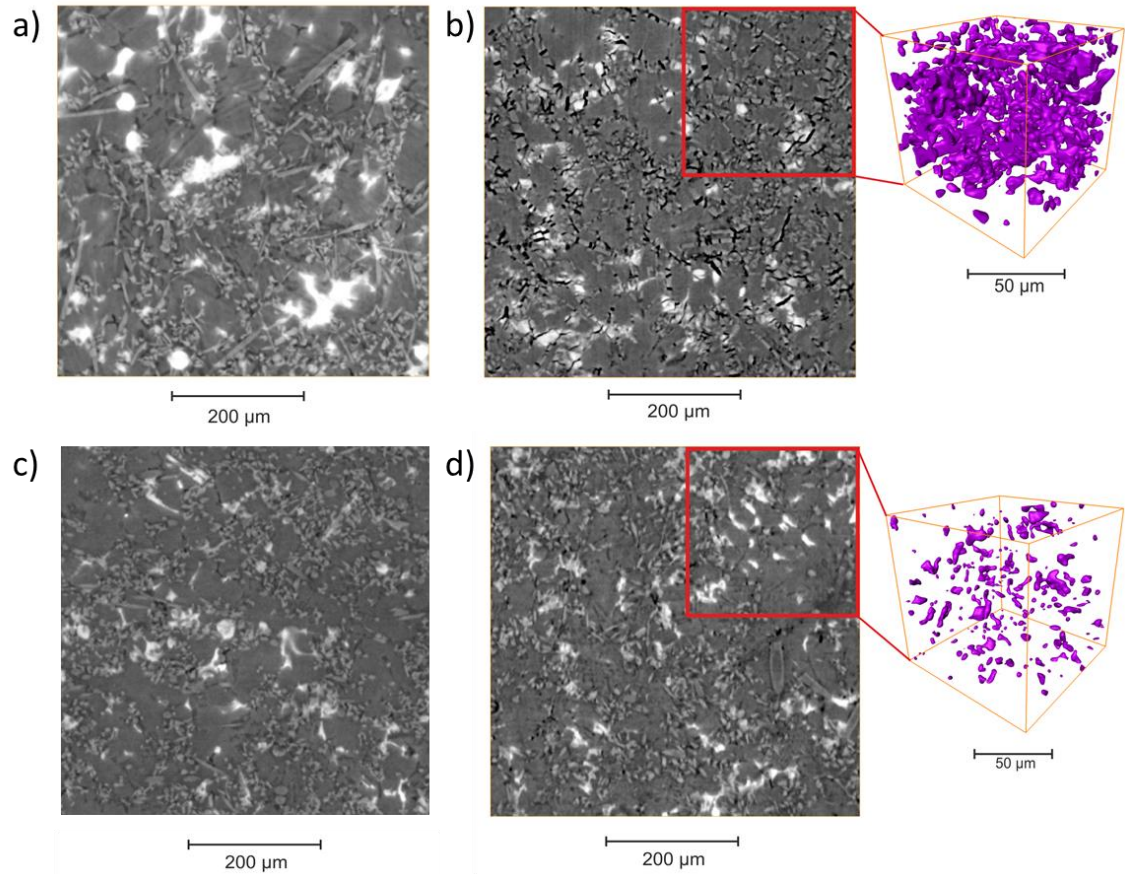


Figure 10. Influence of the SF plane orientation for Type II material: Sections of SXCT reconstructions for (a) initial state for Type II_O; (b) after failure for Type II_O; (c) initial state for Type II_P; (d) after failure for Type II_P.

Figure 11 presents the 3D rendering of SXCT data reconstructions of damage in all composites. As expected, at the same pre-strain Type I_O (Figure 11b) shows higher damage than Type I_P (Figure 11a), due to the more frequent breakage of Al_2O_3 fibers in the latter. In contrast, for Type II the parallel orientation of fibers (Figure 11d) shows larger damage than Type II_O (Figure 11e); this reflects the large amount of damage within the SiC clusters.

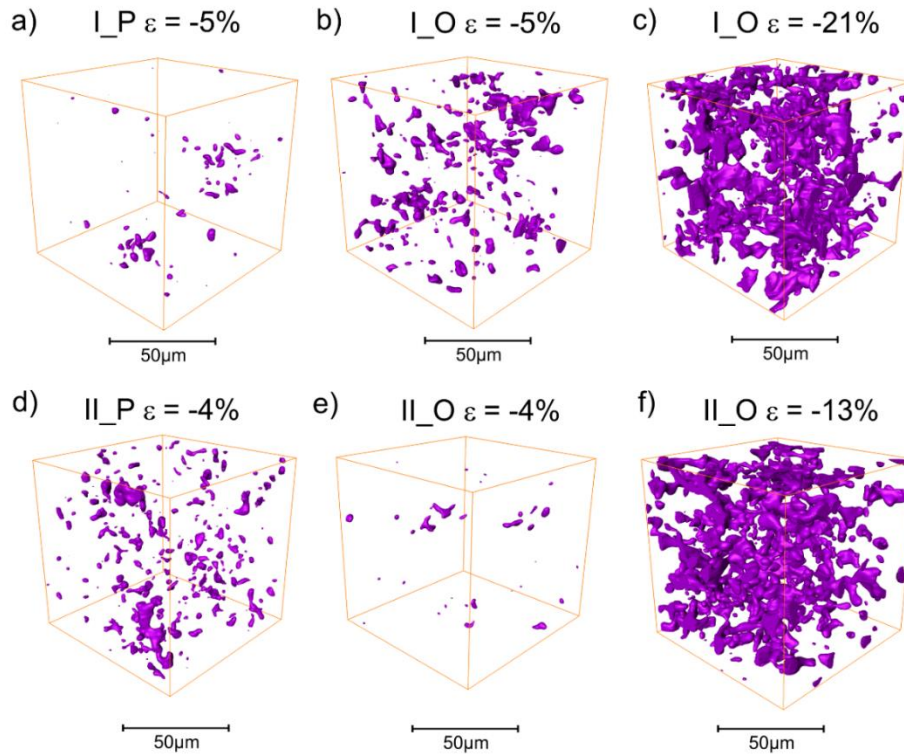


Figure 11. 3D rendering of damage in (a) Type I_P until failure (at $\epsilon=-5\%$), (b) Type I_O at $\epsilon=-5\%$, (c) Type I_O until failure (at $\epsilon=-21\%$); (d) Type II_P until failure (at $\epsilon=-4\%$), (e) Type II_O at $\epsilon=-4\%$, (f) Type II_O until failure (at $\epsilon=-13\%$). Data on Type I are taken from [25], while data on Type I_P and II_P are taken from [15].

Figure 12 summarizes the volume fraction of segmented damage after uniaxial compression for Type I and Type II (both _O and _P samples). Type I_P material has better damage resistance than Type II_P until failure. This is due to its higher volume fraction of Al_2O_3 fibers, which all contribute to withstand the load. In contrast, for the orthogonal configuration, the volume fraction of damage is much smaller for Type II_O than for Type I_O at a pre-strain of about 5%. Therefore, Type II_O is able to accommodate strain more efficiently in the low-plastic strain region. However, at failure, both Type II_O and Type I_O composites reach a similar volume fraction of damage, but Type I_O fails at almost double the strain than Type II_O. This indicates a more catastrophic development of damage as a function of applied pre-strain. Cracking of SiC clusters in Type II_O plays a crucial role (see Figure 3 and 4): since clusters have low aspect ratio, one can think that their rupture is “simultaneous”, since the radial stress component is always normal to the main axis of some clusters. This is not the case in Type I_O.

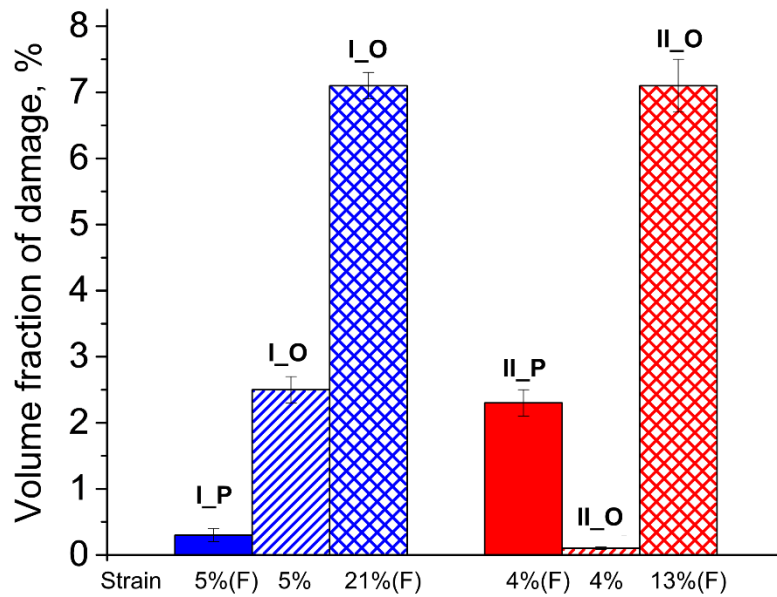


Figure 12. Total volume fraction of segmented voids for samples of the two composites with fibers aligned parallel (P) [25,15] and orthogonal (O) to the compression direction. The strain value for each sample is shown under the column. Note that (F) indicates the failure condition.

Damage in each phase can be rationalized by the proposed analytical model; indeed, the model represents the only approach to obtain all phase-specific principal stresses, in view of the impossibility to extract a strain-free reference for each phase. Those principal stresses for Type I_O (left) and Type II_O (right) are plotted in Figure 13 (the plots also assume no residual stress).

For the Al-phase (Figure 13a, e) the axial direction (σ_1) shows a constant slope. However, for the radial direction (σ_3) -within the plane of Al_2O_3 fibers- there is strain hardening (higher slope) and the phase-specific stress drops above $\sigma^{\text{app}} = -400$ MPa. This may be due to the complex load transfer scenario, where the intermetallic *network* carries increasingly more load, in spite of the damage within particles.

Knowing the principal stresses, we can also state that Type I_O shows higher stress levels in the Al-phase than Type II_O. This is related to the higher volume of ceramic reinforcement of the latter composite. Importantly, we notice that the Al-matrix remains always under increasing compressive stress in all directions. The Poisson's tension in the direction transverse to the load

is carried by the alumina fibers for both composites at the same level (Figure 13c, g). This explains why damage is largely concentrated in the ceramic reinforcements, and the matrix does not suffer any significant micro-cracking (see also [16]). We notice, that in Type II_P, the Al-phase does carry some load in the radial direction (see Figure 8 in [15]). Also, stress levels in the axial direction are almost twice as high for Type I_O as for Type I_P, while Type II_O behaves more similar to Type II_P; this demonstrates the important role of the presence of SiC in the _P composites. The smaller volume fraction of fibers in Type I would not explain those observations (see [5]).

The Si-phase presents a similar tendency for both composites (Figure 13b, f) but at higher applied loads (around -400 MPa) Type I_O seems to carry more load.

For the Al₂O₃ fibers the load carrying capability drastically decreases above $\sigma^{\text{app}} = -350$ MPa for Type I_O and from $\sigma^{\text{app}} = -400$ MPa for Type II_O, but does not vanish. Therefore, Al₂O₃ fibers are still reinforcing but in the guise of particles. Interestingly, we could draw similar conclusions for the Al₂O₃ phase in Type I_P and Type II_P composites [25,15]: when fibers are oriented in the load axis plane, their fragmentation in the transverse in-plane direction renders the response to compression more isotropic (in the other transverse axis, perpendicular to the fiber mats, fibers behave as particles from the very beginning of loading).

The most interesting features are displayed by the intermetallic phases (Figure 13d, h): their response to applied compressive stress is basically linear up to $\sigma^{\text{app}} = -400$ MPa. Above $\sigma^{\text{app}} = -400$ MPa, they carry most of the load (experience the highest stress) in the axial direction in spite of the damage they suffer, and even upon breakage of the ceramic reinforcements (this in fact holds true for both Type I_O and II_O materials). This is only possible considering the interconnectivity of the IM particles with the Si (and with the SiC, for Type II_O). In other words, the IM phases do not contribute as single particles, but as one entity. This has been also observed in the unreinforced alloy [43]. This feature is extremely difficult to model analytically

and is *per se* not contained in our model. Nevertheless, the variation of the aspect ratio, based on SXCT 3D reconstructions, allows mimicking it. At high loads, also the Si phase behaves as an interconnected network, and carries load in spite of particle breakage. It would be interesting to observe this behavior in heat-treated composites, since it has been documented [44,45] that the Si network dissolves upon annealing, *i.e.* Si globularizes. In such a case it would be expected that the strong effect of interconnectivity would disappear, and the reinforcing precipitates would act as isolated particles. This problem is subject of a separate study. In the radial direction, stress in the IM is small, since, as mentioned above, the Al₂O₃ fibers play the main role in the load transfer. In Type II_O, the SiC-phase (Figure 13i) shows a linear response up to $\sigma^{app} = -360$ MPa. At higher applied stresses the effect of damage in SiC clusters reduces the load carrying capability of the SiC (the slope is decreasing). This feature is not present in Type II_P, because in the case when Al₂O₃ fibers are oriented parallel to the applied load axis, fibers remained effective (as such) until total failure of the composites, while in Type II_O they fragment and behave like particles (compare the damage amounts in Figure 10 and 11). This causes the SiC particles to carry higher load and finally break.

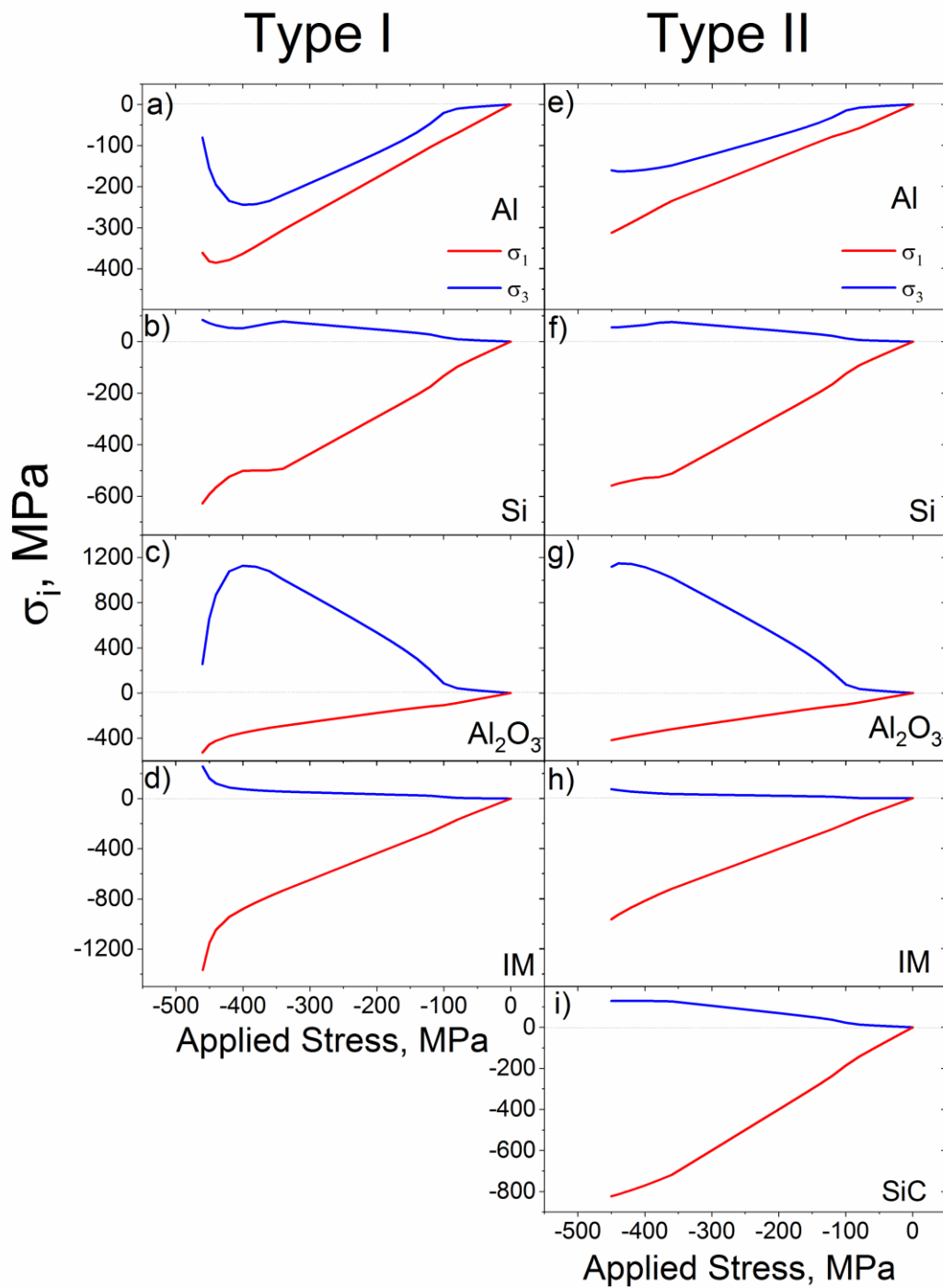


Figure 13. Modeled principal stresses for Type I_O a) Al, b) Si, c) Al₂O₃ fibers, d) intermetallic particles; for Type II_O e) Al, f) Si, g) Al₂O₃ fibers, h) intermetallic particles, i) SiC. Please note the different scale for each phase.

5. Conclusions

We studied the mechanical response of Al-alloy matrix composites with one and two ceramic reinforcing phases (Al₂O₃ planar random oriented fibers and Al₂O₃ fibers with SiC particles)

under uniaxial compression, with the Al_2O_3 fiber mats perpendicular to the load axis. We compared the mechanical behavior of these materials with similar ones, having the Al_2O_3 fiber mat plane containing the load axis, previously reported.

We showed that in composites with the Al_2O_3 fiber mat plane perpendicular to the load axis the Al-alloy matrix presents a large hydrostatic stress component, *i.e.* undergoes compression also in the direction transverse to the external load. This feature holds with and without the addition of SiC ceramic reinforcement and is absent in the case when the Al_2O_3 fiber mat plane is parallel to the load axis. Load in the radial direction is essentially carried by the Al_2O_3 fibers and by the intermetallic network (attached to the Si network and to the SiC particle clusters). We also show here, that the intermetallics play an important role at very high loads, when all other reinforcement phases suffer (extensive) damage. Type II composite presents higher mechanical resistance than Type I when Al_2O_3 fibers are in orthogonal orientation to load; this is opposite to the case when fibers are parallel to the load axis, and is related to the brittle nature of Al_2O_3 phase (more easily breaking under tensile -radial- stresses). The addition of SiC particles does alleviate the load on the Al_2O_3 fibers, on the eutectic Si, and on the intermetallic phases in both cases of parallel and orthogonal (to the load axis) Al_2O_3 fiber orientation, but this effect is much more visible in the parallel case. The addition of SiC particles also renders the mechanical response of such multi-phase composites nearly isotropic, in spite of the presence of random-planar oriented Al_2O_3 fibers.

Acknowledgements.

SE, IS, GG, and GB acknowledge financial support from the DFG (Project number BR 5199/3-1). Authors thank Robert Koos (MLZ/FRMII, TU Munich, Germany) and Robert

Wimpory (HZB, Berlin, Germany) for their support during neutron diffraction measurements on the STRESS-SPEC and E3 beamlines.

Appendix A

The components of Wu's tensor \mathbf{F} for an isolated spheroidal inhomogeneity (with semi-axes $a_1 = a_2 = a, a_3$) of the aspect ratio $\gamma = a/a_3$, with bulk and shear moduli K_1 and G_1 , embedded in the matrix with bulk and shear moduli K_0 and G_0 , are as follows:

$$\begin{aligned}\Gamma_{1111} &= \frac{1}{2\Delta_\Gamma} \left[1 + q_6 \left(K + \frac{4}{3}G \right) + 2q_4 \left(K - \frac{2}{3}G \right) \right] + \frac{1}{2(1+2q_2G)}; \quad \Gamma_{1212} = \frac{1}{2(1+2q_2G)} \\ \Gamma_{1133} &= -\frac{1}{\Delta_\Gamma} \left[2q_1 \left(K - \frac{2}{3}G \right) + q_3 \left(K + \frac{4}{3}G \right) \right]; \\ \Gamma_{3311} &= -\frac{1}{\Delta_\Gamma} \left[2q_4 \left(K + \frac{1}{3}G \right) + q_6 \left(K - \frac{2}{3}G \right) \right] \\ \Gamma_{3333} &= \frac{2}{\Delta_\Gamma} \left[\frac{1}{2} + 2q_1 \left(K + \frac{1}{3}G \right) + q_3 \left(K - \frac{2}{3}G \right) \right]; \quad \Gamma_{1313} = \frac{1}{2(1+q_5G)}\end{aligned}\tag{A.1}$$

where the functions f_0 and f_1 are given by

$$\begin{aligned}f_0 &= \frac{1-g}{2(1-\gamma^2)}, \quad f_1 = \frac{1}{4(1-\gamma^2)^2} \left[(2+\gamma^2)g - 3\gamma^2 \right], \text{ with} \\ g &= \begin{cases} \frac{1}{\gamma\sqrt{1-\gamma^2}} \arctan \frac{\sqrt{1-\gamma^2}}{\gamma}, & (\gamma < 1) \\ \frac{1}{\gamma\sqrt{\gamma^2-1}} \ln \left(\gamma + \sqrt{\gamma^2-1} \right), & (\gamma > 1) \end{cases}\end{aligned}\tag{A.2}$$

and the following notations are used

$$\begin{aligned}q_1 &= G_0 \left[4\kappa - 1 - 2(3\kappa - 1)f_0 - 2\kappa f_1 \right], \quad q_2 = 2G_0 \left[1 - (2 - \kappa)f_0 - \kappa f_1 \right]; \quad q_5 = 4G_0 (f_0 + 4\kappa f_1) \\ q_3 &= q_4 = 2G_0 \left[(2\kappa - 1)f_0 + 2\kappa f_1 \right], \quad q_6 = 8G_0 (\kappa f_0 - \kappa f_1), \\ K &= K_1 K_0 / (K_0 - K_1); \quad G = G_1 G_0 / (G_0 - G_1); \quad \kappa = (3K_0 + G_0) / (3K_0 + 4G_0)\end{aligned}\tag{A.3}$$

$$\Delta_{\Gamma} = 2 \left\{ \left[\frac{1}{2} + 2q_1 \left(K + \frac{1}{3}G \right) + q_3 \left(K - \frac{2}{3}G \right) \right] \left[1 + 2q_4 \left(K - \frac{2}{3}G \right) + q_6 \left(K + \frac{4}{3}G \right) \right] \right. \\ \left. - \left[2q_1 \left(K - \frac{2}{3}G \right) + q_3 \left(K + \frac{4}{3}G \right) \right] \left[2q_4 \left(K + \frac{1}{3}G \right) + q_6 \left(K - \frac{2}{3}G \right) \right] \right\} \quad (\text{A.4})$$

The components of transversely isotropic (x_3 is the axis of symmetry) tensor Q^{Ω} entering (f) are as follows:

$$Q_{1111}^{\Omega} = Q_{2222}^{\Omega} = \mu\kappa(4 - 5f_0 - 3f_1), \quad Q_{1122}^{\Omega} = \mu[4\kappa - 2 + (4 - 7\kappa)f_0 - \kappa f_1] \\ Q_{3333}^{\Omega} = 8\mu\kappa(f_0 - f_1), \quad Q_{1133}^{\Omega} = 2\mu[(2\kappa - 1)f_0 + 2\kappa f_1], \\ Q_{1313}^{\Omega} = \mu(f_0 + 4\kappa f_1) \quad (\text{A.5})$$

where f_0 and f_1 are calculated for the aspect ratio of the domain Ω . In [42] the Maxwell's scheme was completed expressing the aspect ratio the domain Ω in terms of the sums of components of tensors Q_{ijkl} for individual inhomogeneities: for a composite with transversely isotropic microstructure, the effective inclusion is a spheroid with aspect ratio

$$\gamma_{\Omega} = \frac{\sum_i V_i Q_{3333}^{(i)}}{\sum_i V_i Q_{1111}^{(i)}} \quad (\text{A.6})$$

if it is smaller than 1 (case relevant to the present study). This hypothesis was numerically verified in [46].

Procedure of averaging of the transversely-isotropic fourth-rank tensor Γ_{ijkl} over orientations has been discussed in detail in [34]. In the case of 3-D random orientation the resulting tensor is isotropic and has only two independent components

$$\bar{\Gamma}_{1111} = \frac{1}{15}(8\Gamma_{1111} + 2\Gamma_{1133} + 2\Gamma_{3311} + 8\Gamma_{1313} + 3\Gamma_{3333}) \\ \bar{\Gamma}_{1122} = \frac{1}{15}(\Gamma_{1111} + 5\Gamma_{1122} + 4\Gamma_{1133} + 4\Gamma_{3311} - 4\Gamma_{1313} + \Gamma_{3333}) \quad (\text{A.7})$$

Tensor Γ_{ijkl} averaged over 2-D random orientations is transversely isotropic with the axis of symmetry normal to the plane of random orientations. The resulting tensor has six independent components (note that stress concentration tensor is not symmetric and $\bar{\Gamma}_{1133} \neq \bar{\Gamma}_{3311}$):

$$\bar{\Gamma}_{1111} = \frac{1}{8}(-\Gamma_{1111} + 4\Gamma_{1122} + 5\Gamma_{1133} + 5\Gamma_{3311} + 12\Gamma_{1313} + 3\Gamma_{3333});$$

$$\bar{\Gamma}_{3333} = \Gamma_{1111}$$

$$\bar{\Gamma}_{1212} = \frac{1}{8}(-3\Gamma_{1111} + 4\Gamma_{1122} - \Gamma_{1133} - \Gamma_{3311} + 4\Gamma_{1313} + \Gamma_{3333});$$

$$\bar{\Gamma}_{1313} = \Gamma_{1313}$$

$$\bar{\Gamma}_{1133} = \frac{1}{4}(\Gamma_{1111} + \Gamma_{1122} + 4\Gamma_{3311});$$

$$\bar{\Gamma}_{3311} = \frac{1}{4}(\Gamma_{1111} + \Gamma_{1122} + 4\Gamma_{1133}) \tag{A.8}$$

Conflict of Interest:

The authors declare that they have no conflict of interest.

References

1. Clyne TW, Withers PJ (1993) An Introduction to Metal Matrix Composites. Cambridge Solid State Science Series. Cambridge University Press, Cambridge.
2. Dlouhy A, Eggeler G, Merk N (1995) A micromechanical model for creep in short fibre reinforced aluminium alloys. *Acta Metallurgica et Materialia* 43 (2):535-550
3. Dragone TL, Nix WD (1990) Geometric factors affecting the internal stress distribution and high temperature creep rate of discontinuous fiber reinforced metals. *Acta Metallurgica et Materialia* 38 (10):1941-1953
4. Requena G, Degischer HP (2006) Creep behaviour of unreinforced and short fibre reinforced AlSi12CuMgNi piston alloy. *Materials Science and Engineering: A* 420 (1):265-275
5. Garces G, Bruno G, Wanner A (2007) Load transfer in short fibre reinforced metal matrix composites. *Acta Materialia* 55 (16):5389-5400
6. Garces G, Bruno G, Wanner A (2006) Residual stresses in deformed random-planar aluminium/Saffil® short-fibre composites. *Materials Science and Engineering: A* 417 (1):73-81
7. Garces G, Bruno G, Wanner A (2006) Internal stress evolution in a random-planar short fiber aluminum composite. *Scripta Materialia* 55 (2):163-166
8. Michaud V, Mortensen A (2001) Infiltration processing of fibre reinforced composites: governing phenomena. *Composites Part A: Applied Science and Manufacturing* 32 (8):981-996
9. Oh KH, Han KS (2007) Short-fiber/particle hybrid reinforcement: Effects on fracture toughness and fatigue crack growth of metal matrix composites. *Composites Science and Technology* 67 (7):1719-1726
10. Wang Y-q, Song J-i (2011) Dry sliding wear behavior of Al₂O₃ fiber and SiC particle reinforced aluminium based MMCs fabricated by squeeze casting method. *Transactions of Nonferrous Metals Society of China* 21 (7):1441-1448
11. Friend CM, Horsfall I, Burrows CL (1991) The effect of particulate: fibre ratio on the properties of short-fibre/particulate hybrid MMC produced by preform infiltration. *Journal of Materials Science* 26 (1):225-231
12. Mondal AK, Kumar S (2009) Dry sliding wear behaviour of magnesium alloy based hybrid composites in the longitudinal direction. *Wear* 267 (1):458-466
13. Schröder J, Kainer KU (1991) Magnesium-base hybrid composites prepared by liquid infiltration. *Materials Science and Engineering: A* 135:33-36
14. Skleničkal V, Kuchařová K, Kvapilová M, Svoboda M (2015) Factors influencing creep resistance in discontinuously reinforced magnesium metal matrix composites. *Metallic Materials* 53 (4):221-229
15. Cabeza S, Mishurova T, Garces G, Sevostianov I, Requena G, Bruno G (2017) Stress-induced damage evolution in cast AlSi12CuMgNi alloy with one- and two-ceramic reinforcements. *Journal of Materials Science* 52 (17):10198-10216

16. Evsevlev S, Mishurova T, Cabeza S, Koos R, Sevostianov I, Garcés G, Requena G, Fernandez R, Bruno G (2018) The role of intermetallics in stress partitioning and damage evolution of AlSi12CuMgNi alloy. *Materials Science and Engineering: A*
17. Fitzpatrick ME, Withers PJ, Baczmanski A, Hutchings MT, Levy R, Ceretti M, Lodini A (2002) Changes in the misfit stresses in an Al/SiCp metal matrix composite under plastic strain. *Acta Materialia* 50 (5):1031-1040
18. Winand HMA, Whitehouse AF, Withers PJ (2000) An investigation of the isothermal creep response of Al-based composites by neutron diffraction. *Materials Science and Engineering: A* 284 (1):103-113
19. Young ML, Rao R, Almer JD, Haeffner DR, Lewis JA, Dunand DC (2009) Load partitioning in Al₂O₃-Al composites with three-dimensional periodic architecture. *Acta Materialia* 57 2362–2375
20. Roy S, Gibmeier J, Kostov V, Weidenmann KA, Nagelb A, Wanner A (2012) Internal load transfer and damage evolution in a 3D interpenetrating metal/ceramic composite. *Materials Science and Engineering A* 551 272– 279
21. Roy S, Gibmeier J, Kostov V, Weidenmann KA, Nagel A, Wanner A (2011) Internal load transfer in a metal matrix composite with a three-dimensional interpenetrating structure. *Acta Materialia* 59 1424–1435
22. Rack A, Zabler S, Müller BR, Riesemeier H, Weidemann G, Lange A, Goebbels J, Hentschel M, Görner W (2008) High resolution synchrotron-based radiography and tomography using hard X-rays at the BAMline (BESSY II). *Nuclear Instruments and Methods in Physics Research Section A: Accelerators, Spectrometers, Detectors and Associated Equipment* 586 (2):327-344
23. Paganin D, Mayo SC, Gureyev TE, Miller PR, Wilkins SW (2002) Simultaneous phase and amplitude extraction from a single defocused image of a homogeneous object. *J Microsc-Oxford* 206:33-40
24. Weitkamp T, Haas D, Wegrzynek D, Rack A (2011) ANKAphase: software for single-distance phase retrieval from inline X-ray phase-contrast radiographs. *J Synchrotron Radiat* 18:617-629
25. Cabeza S, Mishurova T, Bruno G, Garcés G, Requena G (2016) The role of reinforcement orientation on the damage evolution of AlSi12CuMgNi+15% Al₂O₃ under compression. *Scripta Materialia* 122:115-118
26. Hoelzel M, Gan W, Hofmann M, Randau C, Seidl G, Juttner P, Schmahl W (2013) Rotatable multifunctional load frames for neutron diffractometers at FRM II-design, specifications and applications. *Nuclear Instruments & Methods in Physics Research Section a-Accelerators Spectrometers Detectors and Associated Equipment* 711:101-105
27. Wern H (2000) XEC. 1.0 edn. Hochschule für Technik und Wirtschaft Saarbrücken.
28. Kröner E (1958) Berechnung der elastischen Konstanten des Vielkristalls aus den Konstanten des Einkristalls. *Zeitschrift für Physik* 151 (4):504-518
29. Hutchings MT, Krawitz AD (1992) *Measurement of Residual and Applied Stress Using Neutron Diffraction*. Springer Netherlands.
30. Garcés G, Bruno G, Wanner A (2006) Residual stresses in random-planar aluminium/Saffil short-fibre composites deformed in different loading modes. *Journal of Materials Research* 97 (10):1312-1319
31. Dutta M, Bruno G, Edwards L, Fitzpatrick ME (2004) Neutron diffraction measurement of the internal stresses following heat treatment of a plastically deformed Al/SiC particulate metal–matrix composite. *Acta Materialia* 52 (13):3881-3888
32. Bruno G, Ceretti M, Girardin E, Giuliani A, Manescu A (2004) Relaxation of residual stress in MMC after combined plastic deformation and heat treatment. *Scripta Materialia* 51:999–1004
33. Sevostianov I, Giraud A (2013) Generalization of Maxwell homogenization scheme for elastic material containing inhomogeneities of diverse shape. *International Journal of Engineering Science* 64 (Supplement C):23-36
34. Mishurova T, Cabeza S, Bruno G, Sevostianov I (2016) Average phase stress concentrations in multiphase metal matrix composites under compressive loading. *International Journal of Engineering Science* 106:245-261

35. Fernández-Gutiérrez R, Requena GC (2014) The effect of spheroidisation heat treatment on the creep resistance of a cast AlSi12CuMgNi piston alloy. *Materials Science and Engineering: A* 598 (Supplement C):147-153
36. Chen CL, Richter A, Thomson RC (2010) Investigation of mechanical properties of intermetallic phases in multi-component Al–Si alloys using hot-stage nanoindentation. *Intermetallics* 18 (4):499-508
37. Sevostianov I, Kachanov M (2015) On the possibility to represent effective properties of a material with inhomogeneities in terms of concentration parameters. *International Journal of Solids and Structures* 52 (Supplement C):197-204
38. Hill R (1963) Elastic properties of reinforced solids: Some theoretical principles. *Journal of the Mechanics and Physics of Solids* 11 (5):357-372
39. Wu TT (1966) The effect of inclusion shape on the elastic moduli of a two-phase material. *International Journal of Solids and Structures* 2 (1):1-8
40. Chen F, Sevostianov I, Giraud A, Grgic D (2017) Accuracy of the replacement relations for materials with non-ellipsoidal inhomogeneities. *International Journal of Solids and Structures* 104 (Supplement C):73-80
41. Maxwell JC (1873) *A treatise on electricity and magnetism*. Clarendon Press, Oxford.
42. Sevostianov I (2014) On the shape of effective inclusion in the Maxwell homogenization scheme for anisotropic elastic composites. *Mechanics of Materials* 75 (Supplement C):45-59
43. Evsevlev S, Mishurova T, Cabeza S, Koos R, Sevostianov I, Garcés G, Requena G, Fernández R, Bruno G (2018) The role of intermetallics in stress partitioning and damage evolution of AlSi12CuMgNi alloy. *Materials Science and Engineering: A* 736:453-464
44. Requena G, Garcés G, Rodríguez M, Pirling T, Cloetens P (2009) 3D Architecture and Load Partition in Eutectic Al-Si Alloys. *Advanced Engineering Materials* 11 (12):1007-1014
45. Bugelnig K, Sket F, Germann H, Steffens T, Koos R, Wilde F, Boller E, Requena G (2018) Influence of 3D connectivity of rigid phases on damage evolution during tensile deformation of an AlSi12Cu4Ni2 piston alloy. *Materials Science and Engineering: A* 709 (Supplement C):193-202
46. Kushch VI, Sevostianov I (2016) Maxwell homogenization scheme as a rigorous method of micromechanics: Application to effective conductivity of a composite with spheroidal particles. *International Journal of Engineering Science* 98 (Supplement C):36-50